

Critical Role of Polystyrene Layer on Plasmonic Silver Nanoplates in Organic Photovoltaics

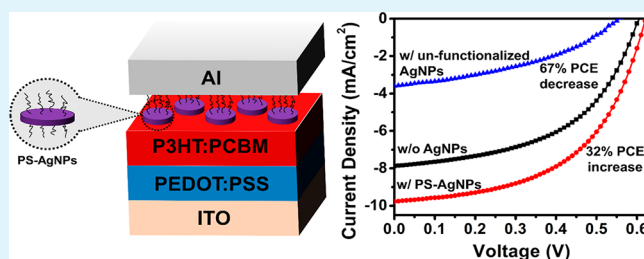
Jonathan S. Metzman,[†] Assad U. Khan,[‡] Brenden A. Magill,[§] Giti A. Khodaparast,[§] James R. Heflin,^{*,§,||} and Guoliang Liu^{*,‡,||,⊥}

[†]Department of Materials Science and Engineering, [‡]Department of Chemistry, [§]Department of Physics, ^{||}Division of Nanoscience, and [⊥]Macromolecules Innovation Institute, Virginia Tech, Blacksburg, Virginia 24061, United States

Supporting Information

ABSTRACT: Plasmonic nanoparticles create large local electric field enhancements in organic photovoltaics (OPVs), substantially enhance the absorption of light, and consequently improve the device efficiency. In this report, anisotropic Ag nanoplates (AgNPs) were functionalized by thiol-terminated polystyrene (PS-SH) to yield polystyrene-functionalized Ag nanoplates (PS-AgNPs). The PS-AgNPs were spin-coated directly on the OPV active layer, poly(3-hexylthiophene-2,5-diyl):[6,6]-phenyl C₆₁ butyric acid methyl ester (P3HT:PCBM). A systematic variation of the PS-AgNP solution concentration correlated to different nanoparticle densities on the active layer. The localized surface plasmon resonance (LSPR) of the PS-AgNPs enhanced the light absorption of the active layer, which directly contributed to an increase in exciton yield, demonstrated by the increased photoluminescence emission intensities in P3HT films. In addition, incorporation of the PS-AgNPs decreased the series resistance and increased the photocurrent of the devices. In devices with PS-AgNP at a concentration of 0.57 nM, the power conversion efficiency was 32% higher than the devices without the PS-AgNPs. Without the polystyrene functionalization, however, the AgNPs severely deteriorated the performance of the OPV devices regardless of the nanoparticle concentration.

KEYWORDS: plasmonic nanoparticle, polystyrene, functionalization, organic photovoltaics, dispersion



INTRODUCTION

Organic photovoltaics (OPVs) are attractive renewable energy conversion devices due to the relative low-cost, ease of large-scale fabrication, solution processability, flexibility, and light weight.^{1,2} The introduction of bulk heterojunctions (BHJ) dramatically improved the performance of OPVs through the formation of interpenetrated phases of conjugated polymers (electron donor) and fullerene derivatives (electron acceptor). The interpenetrated phases have a high interfacial area and small domains for efficient exciton diffusion and dissociation.^{1,2} Recently, single-junction BHJ OPVs with narrow-bandgap materials have demonstrated power conversion efficiencies that meet the critical benchmark for commercialization viability.^{3–5} However, despite the improvements to donor/acceptor materials^{3–5} and morphology of the active layer,^{6–10} the power conversion efficiency (PCE) of OPV devices is still restrained by limitations on exciton diffusion lengths, charge carrier mobilities, and optical absorption efficiency.^{1,2}

The addition of plasmonic nanoparticles to OPV devices is a promising approach to increasing the optical absorption without modifications to the active layer.¹¹ The exposure of incident light onto plasmonic nanoparticles induces resonance of the conduction electrons within their metallic core, which creates local electric field enhancements in the vicinity of the nanoparticles, often termed localized surface plasmon reso-

nance (LSPR).^{12–15} When the nanoparticle LSPR frequency couples with the OPV absorption frequency, the OPV optical absorption can be substantially improved. The characteristic LSPR frequency is dependent on the nanoparticle composition, size, shape, aspect ratio, and the refractive index of the surrounding medium.^{12–15} Studies have shown that the extinction of small nanoparticles (<20 nm) arise strongly from their absorption (optical loss), while large nanoparticles (>50 nm) possess dominant light-scattering contributions.^{12,16,17} The scattering increases the path length of light within the OPV device and thus induces improved light absorption by the active layer.¹⁸ Among all noble metals, silver (Ag) has superior scattering efficiency, low radiative damping, and low interband losses in the visible wavelength range.^{19–21} In addition, Ag is substantially less expensive than gold.²⁰ Compared to spheres, anisotropic Ag nanoparticles are excellent for OPVs due to the high extinction efficiencies (the ratio of extinction cross section to effective area).²² In particular, nanoprisms are the most attractive because of the large local field enhancements at the triangular tips.^{12,13,22}

Received: October 27, 2018

Accepted: March 11, 2019

Published: March 11, 2019

The nanoparticle location in the OPV device is crucial. Nanoparticles can be positioned within OPV devices at virtually any layer or interface. For instance, the hole-collecting buffer layer, poly(3,4-ethylenedioxythiophene):poly(styrene-sulfonate) (PEDOT:PSS), is widely used as a location for plasmonic nanoparticles.^{17,19,23–27} Although the aqueous PEDOT:PSS mixtures are miscible with hydrophilic plasmonic nanoparticles, the electrical conductivity of PEDOT:PSS requires highly acidic conditions ($\text{pH} \approx 1.6$),²⁸ which cause rapid deterioration of Ag nanoparticles (based on our own trials). Nanoparticles added directly to the active layer have the closest proximity to the light absorbing donor/acceptors and so in principle should yield the largest device improvements. However, nanoparticles coated with short-chain ligands,^{29,30} thiols,^{31,32} or surfactants³³ added to the active layer have been repeatedly shown to increase exciton quenching and nonradiative charge carrier recombination, both of which are detrimental to the device performance.^{16,17} Charge carrier recombination in the active layer can be avoided if nanoparticles are coated with insulating oxides,^{31,34} or are synthesized by laser ablation to be surfactant-free,^{33,35} but these methods are time-consuming and difficult. Alternatively, the incorporation of the plasmonic nanoparticles directly outside the active layer (i.e., at the organic/electrode interfaces^{24,36–38}) can mitigate the recombination effect while still providing strong performance enhancements.

In addition to the location, nanoparticle dispersion within OPV devices is also crucial to avoid performance degradation.^{19,30,32,39} Coating nanoparticles with high-molecular-weight polymers^{23,40–42} is a facile method for effective nanoparticle dispersion and deterrence of charge carrier recombination. The polymer chains prevent detrimental aggregation of nanoparticles due to steric repulsion.^{43–45} Because thiol has an affinity for and reacts with the Ag nanoparticle surface, thiol-terminated polystyrene (PS-SH) can be “grafted-to” the Ag nanoparticles and create a hydrophobic polystyrene (PS) layer surrounding the nanoparticles. The protective PS layer provides the nanoparticles with long-term dispersion stability in organic solvents, which otherwise is difficult.^{43–45}

Previously, Ag nanospheres functionalized by PS were successfully added into the active layer with controlled dispersion to obtain effective plasmonic enhancements.⁴¹ The polystyrene layer provides an insulating layer and prevents parasitic charge recombination.⁴⁰ However, to our knowledge, it is unknown how two-dimensional Ag nanoplates on the active layer affect the OPV performance. In addition, there are limited reports related to the effects of adding as-synthesized nanoparticles without an appropriate polymer coating into OPVs. A side-by-side systematic comparison of functionalized to unfunctionalized nanoparticles of various concentrations is critical for the utilization of these materials in OPVs. An analysis that experimentally conveys the importance of a specific polymer coating is vital for future work in this field.

In this work, we investigate the role of PS functionalization on the anisotropic Ag nanoplates, which are incorporated at the active layer/cathode interface in OPV devices. We systematically examine the effect of the PS-functionalized Ag nanoplates (PS-AgNPs) concentration on light absorption and steady-state photoluminescence of the active layer as well as the improvements to the PCE of the OPV devices. Finally, we discuss the importance of PS functionalization and its effect on the reduction of exciton quenching and charge trapping, in

addition to various OPV parameters including series resistance, shunt resistance, fill factor, short circuit current, and open circuit voltage.

EXPERIMENTAL SECTION

Synthesis of Ag Nanoplates (AgNPs). AgNPs were synthesized via a seed-mediated method following previous reports with slight modifications.^{14,31,46,47} To prepare Ag seeds, 4.5 mL of ultrapure deionized (DI) water (resistivity, 18.2 $\text{M}\Omega\cdot\text{cm}$) was mixed vigorously with 0.5 mL of 25 mM sodium citrate tribasic dihydrate ($\geq 99.0\%$) and 0.25 mL of 0.5 mM poly(sodium 4-styrenesulfonate) (PSSS; $M_w \sim 1000 \text{ kg mol}^{-1}$) aqueous solutions. Next, 0.3 mL of 10 mM ice-cold sodium borohydride (NaBH_4 ; $\geq 99.99\%$) solution was introduced, followed by the addition of 5 mL of 0.5 mM silver nitrate (AgNO_3 ; $\geq 99.9999\%$) at a rate of 2 mL/min using a syringe pump. Once all of the AgNO_3 was added, the seed solution was stirred for ~ 2 min and then ready for use in the next step.

To synthesize AgNPs, 75 μL of 10 mM ascorbic acid ($\geq 99.0\%$) solution was added to 10 mL of DI water, and a certain volume (75–175 μL) of Ag seed solution was added to the growth solution under vigorous stirring. Immediately afterward, 3 mL of 0.5 mM AgNO_3 was dispensed into the growth solution at a rate of 1 mL/min using a syringe pump. The solution initially appeared yellow, then changed rapidly, and eventually stabilized toward the completion of the growth. Promptly following the complete addition of AgNO_3 , 0.5 mL of 25 mM sodium citrate was added to stabilize the AgNPs. The AgNP synthesis was reiterated with different volumes of Ag seed solutions to synthesize AgNPs of different sizes and λ_{LSPR} . After synthesis, the solutions were sealed and stored in the dark.

Synthesis of Thiol-Terminated Polystyrene (PS-SH). PS-SH was synthesized by reversible addition–fragmentation chain transfer (RAFT) polymerization and subsequent reduction of thiocarbonylthio to thiol (Figure S1). Briefly, styrene (144 mmol) and 2-phenyl-2-propyl benzodithioate (CDB) (0.481 mmol) were mixed in a Schlenk flask using a stirring bar. The mixture in the Schlenk flask was degassed through three freeze–pump–thaw cycles. The Schlenk flask was filled with N_2 and immersed into an oil bath at 110 $^\circ\text{C}$. After heating and stirring for 18 h, the reacted mixture was cooled to room temperature. The resulting CDB-terminated polystyrene (PS-CDB) was precipitated in methanol twice and then dried in a vacuum oven for 24 h. Based on size exclusion chromatography (SEC), the PS-CDB had a molecular weight (M_n) of ~ 10.3 kDa and a polydispersity index of 1.1.

To convert PS-CDB to PS-SH, 1000 mg of PS-CDB was dissolved in 25 mL of THF in a round-bottom flask and mixed with 50 mol equiv (44.51 mg) of NaBH_4 dissolved in 2.4 mL of water. This solution was then stirred vigorously at room temperature for 24 h (Figure S2).⁴⁸ The resulting PS-SH was precipitated in methanol twice and dried in a vacuum oven at room temperature for 48 h. The conversion of PS-CDB to PS-SH was confirmed by NMR (Figure S3).

Functionalization of AgNPs with PS-SH and Their Dispersion in MeOH. A solution of AgNPs was centrifuged at 10000 rpm for 30 min. The supernatant was immediately removed, and the precipitate was redispersed in an identical volume of *N,N*-dimethylformamide (DMF; Certified ACS; $\geq 99.8\%$). Next, PS-SH powder was added to the DMF solution that contained redispersed AgNPs. The final polymer concentration was 0.1 wt % (1 mg/mL). After brief sonication, the solution was gently agitated by a vortex mixer for 24 h to make sure PS-SH fully reacted with the AgNPs. After 24 h, the PS-SH functionalized AgNPs (denoted as PS-AgNPs) were stored in the dark and used within 3 days.

Before use in the photovoltaic devices, PS-AgNPs in DMF were centrifuged at 10000 rpm for 30 min. The supernatant was removed, and the precipitate was redispersed in 500 μL of methanol (MeOH; $\geq 99.9\%$). Because the starting concentration of AgNPs in DMF was 0.57 nM and the final volume of the MeOH solution was maintained at a constant of 500 μL , the final nanoparticle concentration depended on the initial volume of the PS-AgNP solution. For example, with starting volumes of 250, 500, 1000, and 2500 μL PS-

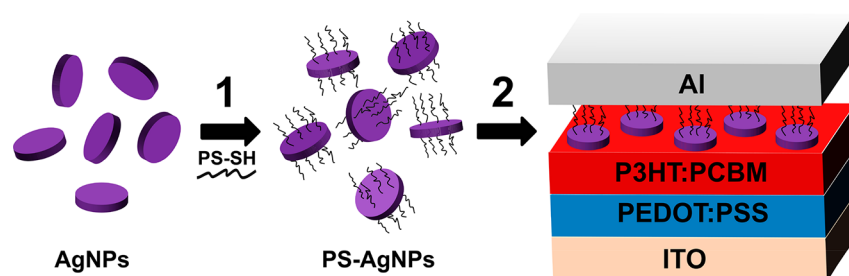


Figure 1. Schematic illustration of an OPV device with PS-AgNPs. The AgNPs are (1) functionalized with a layer of thiol-terminated polystyrene (PS-SH). The PS-AgNPs are (2) deposited on top of the active layer (P3HT:PCBM) in OPV devices.

AgNP solutions in DMF, the final concentrations of PS-AgNPs in MeOH were 0.29, 0.57, 1.14, and 2.90 nM, respectively. After the addition of MeOH, the solution was vortex-mixed and used immediately.

Preparation of ITO Substrate. Float glass slides (resistance, 8–12 ohm; size, 25 × 75 × 0.9 mm³) with indium tin oxide (ITO) on one side and antireflection coating (ARC) on the other side were purchased from Delta Technologies Limited (CH-50IN-S109). The glass slides were vigorously cleaned with acetone (Certified ACS; ≥99.5%) before use. Two electrical tape strips (12.7 mm wide) were applied in the middle of the glass slides along the longitudinal direction to protect the ITO and ARC from etching. The glass slides were then immersed in a mixture of hydrochloric acid (12.1 M) and DI water (HCl: H₂O = 1:1 volume mix ratio) for 1 h to etch the exposed ITO and ARC. The slides were then copiously rinsed with DI water, and the electrical tape was removed to uncover the ITO and ARC (Figure S4, blue stripe). The slides were further cleaned by sonicating in a mixture of 11 mL of hydrogen peroxide (H₂O₂, 30 wt %), 18 mL of ammonium hydroxide (NH₄OH, 30%), and 97 mL of DI water. The ITO slides were then cut into small substrates (size: 25 × 25 mm²), cleaned with acetone and 2-propanol (IPA; Certified ACS; ≥99.5%), and then dried in a stream of nitrogen gas.

Fabrication of Photovoltaic Devices. Poly(3,4-ethylenedioxythiophene):poly(styrenesulfonate) (PEDOT:PSS; Heraeus; CLEVIOS P VP Al 4083) was filtered through a 0.45 μm PVDF syringe filter and vortex-mixed with IPA (PEDOT:PSS/IPA = 3/1, by volume). Solutions of poly(3-hexylthiophene-2,5-diyl) (P3HT, Rieke Metals) and [6,6]-phenyl C₆₁ butyric acid methyl ester (PCBM, Nano-C) at 3 wt % each in anhydrous chlorobenzene (Sigma-Aldrich; ≥99.8%) were prepared separately and stirred overnight at 70 °C. After cooling to room temperature, the two solutions were mixed at a volume ratio of P3HT:PCBM = 1:0.8 and then stirred at 70 °C in the dark before use.

The PEDOT:PSS solution was spin-coated onto an ITO substrate at 4000 rpm for 60 s to obtain a thickness of ~30 nm (as measured by profilometry). The PEDOT:PSS film was then annealed at 140 °C for 20 min in air to remove the solvent. The P3HT:PCBM solution was cooled to room temperature and then spin-coated on top of the PEDOT:PSS film at 1500 rpm for 30 s. For consistency, the P3HT:PCBM films were maintained at a constant thickness of 100 nm for all devices. The active layer thickness of 100 nm was chosen after a systematic investigation and optimization of this parameter (Figure S5 and Table S1). A PS-AgNP solution in MeOH of a desired concentration was spin-coated on top of the active layer at 800 rpm for 60 s. The entire sample was then annealed at 100 °C for 5 min in an argon-filled box. After annealing, the sample was loaded into a thermal evaporator to deposit an aluminum (Al) layer (thickness ~100 nm) at an ultrahigh vacuum of 2 μTorr. The sample holder in the thermal evaporator featured an Al shadow mask to create an active area of 0.12 cm² (Figure S4). After evaporation of Al, the samples were annealed at 130 °C for 15 min under argon.

Instrumentation and Characterization. The transmittance (*T*) and reflectance (*R*) spectra were recorded by a Filmetrics F10-VC-EXR spectrometer. The absorbance (*A*) spectra were calculated according to Beer–Lambert’s law

$$A = -\log\left(\frac{T}{1-R}\right) \quad (1)$$

where *T* and *R* are the transmittance and reflectance at a given wavelength. The absorption spectrum of P3HT:PCBM was obtained by subtracting the absorbance spectrum of glass/ITO/PEDOT:PSS from that of glass/ITO/PEDOT:PSS/P3HT:PCBM. A Veeco DekTak 150 Stylus profilometer was used to measure the thickness of PEDOT:PSS and P3HT:PCBM films. By measuring the thickness of the P3HT:PCBM films, the absorption coefficient (*α*) of P3HT:PCBM was calculated by

$$\alpha = \frac{\ln(10)A}{l} \quad (2)$$

where *l* is the thickness of the film. The absorption coefficient is dependent on wavelength, as shown in Figure S6. With the calculation of the absorption coefficient, the thickness of the P3HT:PCBM films could be calculated from eq 2.

A field-emission scanning electron microscope (SEM, LEO 1550) with an accelerating voltage of 5 kV was used to image the films. An atomic force microscope (AFM, Veeco SPI 3100) with a scan rate of 1 Hz was used to determine the surface roughness of the films after annealing. Transmission electron microscopy (TEM) images were collected on a Phillips EM420 with an accelerating voltage of 120 kV. At least 100 AgNPs were surveyed using ImageJ to gain an estimate of the edge length and thickness.

Photoluminescence (PL) was excited by a continuous wave laser at 488 nm (Coherent Sapphire 488-20). The laser power was 28 mW supplied by a Coherent sapphire LP/SF driver unit. The PL was delivered to a 0.55 m focal length spectrometer (HORIBA Jobin Yvon iHR550) with a 0.1 mm slit width and a 600 grooves/mm, 500 nm blaze grating. The PL was recorded by a liquid nitrogen cooled, charge-coupled device (HORIBA Jobin Yvon Symphony II).

Photovoltaic devices were illuminated to an air mass 1.5 global standard spectrum (AM1.5G) created by a 300 W Xe lamp (Oriel Instruments) with appropriate filters. The intensity was adjusted to 100 mW/cm² (1 sun) as measured with a calibrated silicon photodiode. The current density (*J*)–voltage (*V*) characteristics were evaluated on a Keithley 236 source meter. To measure the external quantum efficiency (EQE), a CVI CM 110 monochromator with 2400 grooves/nm grating was used to filter the light to a specific wavelength in the wavelength range of 300–700 nm. A Keithley 485 picoammeter was used to measure the short-circuit current of the devices. A silicon photodiode was used to measure the input optical power, which was converted to the number of photons at each wavelength. The EQE spectra were obtained by determining the number of electrons divided by the number of photons.

RESULTS

Synthesis and Functionalization of AgNPs. AgNPs were functionalized with thiol-terminated polystyrene. The resulting PS-AgNPs were dispersed in methanol (MeOH) and spin-coated directly on top of the active layer (Figure 1). The placement of the PS-AgNPs between the active layer and the

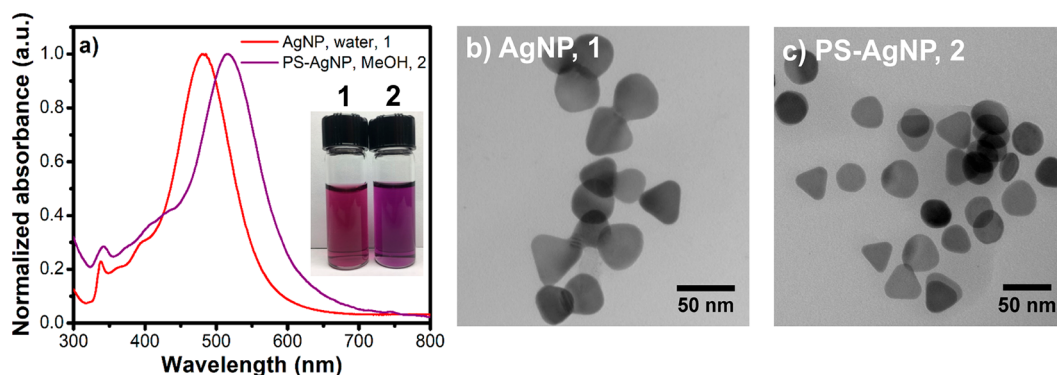


Figure 2. Characterization of AgNPs. (a) Normalized optical absorption spectra of the AgNPs in solution before and after functionalization with PS-SH. The unfunctionalized AgNPs and PS-AgNPs were suspended in water and methanol, respectively. Inset: a photograph of colloidal suspensions of AgNPs (1) and PS-AgNPs (2). (b, c) TEM images of the AgNPs and PS-AgNPs.

electrode is advantageous because (1) the density of the PS-AgNPs can be easily tuned by the nanoparticle solution concentration and (2) the exciton quenching and charge trapping are potentially low compared to placing them in the active layer.¹⁷

To effectively enhance the optical absorption of the active layer, the LSPR of the AgNPs should couple with the absorption peak (λ_{\max}) of P3HT:PCBM. AgNPs with an LSPR peak wavelength (λ_{LSPR}) of 485 nm were synthesized in an aqueous solution (Figure 2a). As measured with TEM (Figure 2b), the AgNPs were primarily nanoplates with an average lateral dimension of 28.3 ± 4.9 nm and an average thickness of 8.6 ± 2.1 nm. Anisotropic AgNPs were selected over spherical particles because the λ_{LSPR} is easily tunable in the visible light range.¹⁶ In addition, the prismatic features in a portion of the AgNPs can further improve the local electric field enhancement effect.^{12,13,22}

To place the AgNPs on the organic active layer of P3HT:PCBM (Figure 1), it is crucial to control the hydrophobicity of the AgNPs.^{34,41} The AgNPs were functionalized with PS-SH in DMF to achieve hydrophobicity. DMF was chosen because both AgNPs and PS-SH are miscible in DMF to allow PS-SH to react with AgNPs.⁴⁹ After functionalization, a layer of polymer was anchored on the AgNPs. The polymer layer enabled the AgNPs to be fully dispersible, with long-term stability, in organic solvents and prevented aggregation.^{43–45} TEM revealed that the PS-AgNPs had a shape similar to the unfunctionalized ones (Figure 2c), indicating that the shape was not compromised during functionalization. The size of the nanoparticles did not change significantly, as confirmed by the size distributions before and after functionalization (Figure S7). The radius of gyration (R_g) is ~ 3.58 nm for polystyrene with a molecular weight of 10.3 kDa.⁵⁰ In a good solvent such as chloroform, the thickness of the polymer layer on the AgNPs ranged from 4 to 5 nm (Figure S8), indicating that the polymer chains were not fully extended but occupied a space slightly larger than R_g similar to our previous report.⁵¹ Based on the studies by Rang et al.⁵² and Haes et al.,⁵³ the optical near field was observed up to 30 nm near the nanoparticles. Therefore, the encapsulation of the AgNPs with PS did not deteriorate the device performance, and the LSPR effects were fully utilized.

The solvent vapor pressure is critical to ensure effective spin-coating.⁵⁴ MeOH has a vapor pressure of 13.01 kPa at room temperature,⁵⁵ which is 2 orders of magnitude higher than that of DMF (0.32 kPa).⁵⁶ Therefore, the PS-AgNPs were

dispersed in MeOH for fast drying after spin-coating, good surface coverage, and minimal nanoparticle aggregation.⁵⁴ Moreover, MeOH is a poor solvent for P3HT:PCBM,¹⁰ and thus it has little influence on the active layer during spin-coating (Figure S9). When dispersed in MeOH, the λ_{LSPR} of the AgNPs red-shifted from 485 to 515 nm (Figure 2a) due to a change in the refractive index ($n_{\text{water}} = 1.34$, $n_{\text{PS}} = 1.60$, and $n_{\text{MeOH}} = 1.35$).⁴³ The λ_{LSPR} of PS-AgNPs at 515 nm closely matched the optical absorption peak of P3HT ($\lambda_{\max} = 514$ nm).

Density and Structures of PS-AgNPs in Thin Films.

The PS-AgNPs were spin-coated on the active layer of P3HT:PCBM. The surface density of the PS-AgNPs was controlled by the solution concentration. As the concentration of the PS-AgNP solution was increased, the density of the PS-AgNPs on the active layer increased (Figure 3). The PS-AgNP

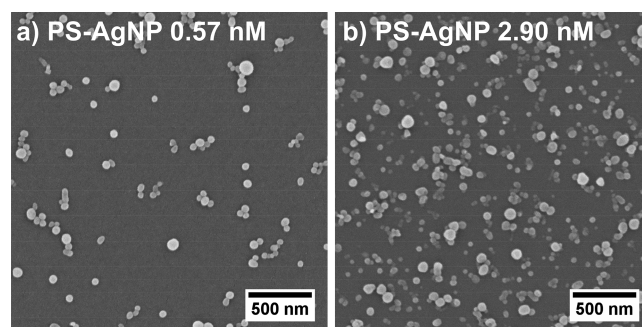


Figure 3. Representative SEM images of PS-AgNPs in OPV devices. The PS-AgNPs were spin-coated on the active layer of P3HT:PCBM from solution concentrations of (a) 0.57 nM and (b) 2.90 nM.

solution of 0.57 nM resulted in a low surface coverage density at $\sim 1.46 \times 10^{10}$ particles/cm² along with a minimal stacking of nanoparticles. At a PS-AgNP solution concentration of 2.90 nM, the surface density reached 3.74×10^{10} particles/cm², and the stacking of PS-AgNPs was clearly observed. Thin films of P3HT:PCBM with PS-AgNPs were then thermally annealed and inspected (Figure S10). The AFM images show that after annealing, the PS-AgNPs remained dispersed on the P3HT:PCBM layer. Additionally, the mean roughness (R_a) and the root-mean-square roughness (R_q) increased with an increasing PS-AgNP concentration (Table S2) due to the increasing nanoparticle density on the active layer.

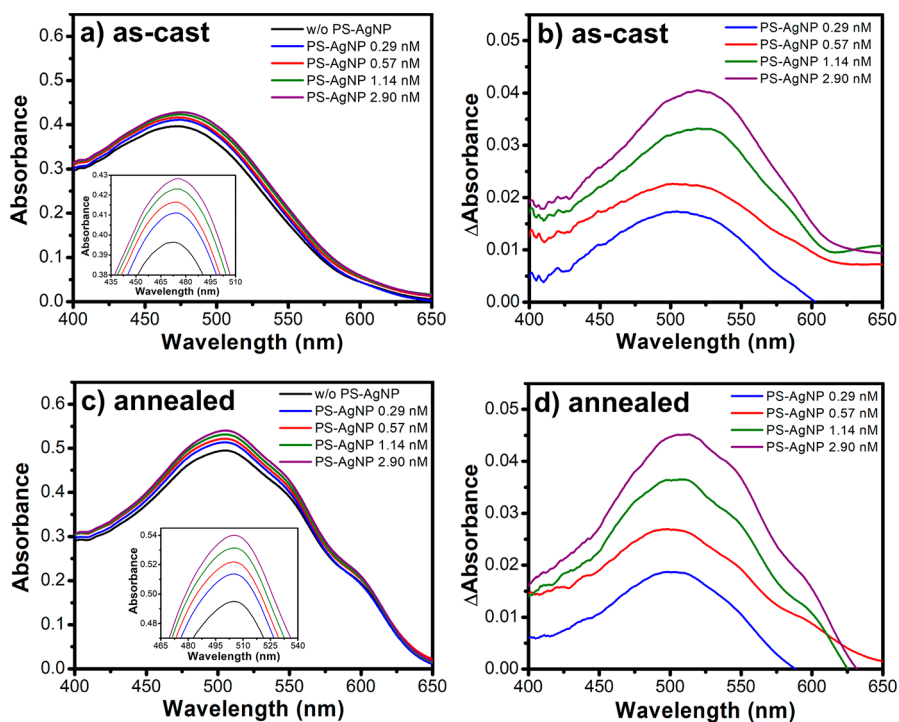


Figure 4. (a) Optical absorption spectra of the as-cast P3HT:PCBM films before and after spin-coating PS-AgNPs. The PS-AgNP solutions had concentrations of 0.29, 0.57, 1.14, and 2.90 nM. (b) Optical absorption difference (Δ Absorbance) between the P3HT:PCBM films with PS-AgNPs and the as-cast P3HT:PCBM films. (c, d) Optical absorption spectra and the difference of the same P3HT:PCBM films after thermal annealing. The insets are zoomed-in view of the absorption peaks.

Enhancement of Optical Absorption. The addition of PS-AgNPs enhanced the optical absorption of the active layer. Figure 4a represents the optical absorption of an as-cast active layer of P3HT:PCBM as well as active layers with PS-AgNPs that were spin-coated from solutions of various concentrations. The optical absorption peak (λ_{max}) of P3HT:PCBM at a mixing ratio of 1:0.8 was at 473 nm, which results from the combined absorption of P3HT ($\lambda_{\text{max}} = 514$ nm) and PCBM ($\lambda_{\text{max}} \approx 340$ nm). The optical absorption intensity increased continuously as the concentration of PS-AgNPs was increased, similar to that in previous reports.^{16,19} For comparison, the PS-AgNPs were spin-coated on pristine P3HT without PCBM. The absorption of P3HT was also enhanced with an increasing concentration of the PS-AgNPs (Figure S11). The absorption difference spectra (Figure 4b) were calculated by subtracting the absorption of P3HT:PCBM from that of the as-cast P3HT:PCBM with PS-AgNPs. The peak positions of the absorption difference spectra were close to the λ_{LSPR} of the PS-AgNPs, suggesting that the absorption enhancements were correlated to the presence of the plasmonic nanoparticles.

Thermal annealing of P3HT:PCBM induces further phase separation of P3HT and PCBM, which also increases the planar ordering of P3HT chains and the crystallinity of P3HT:PCBM.^{6–9} As a result, thermal annealing often improves the optical absorption, photocurrent, charge carrier mobility, and ultimately device performance.^{6–9,57} As shown in Figure 4c, the peak optical absorption of P3HT:PCBM increased from 0.39 to 0.49 after annealing. In addition, the absorption peak wavelength (λ_{max}) red-shifted from 473 to 505 nm (Figure 4c) due to the prominent 0–2 vibronic transition of P3HT.⁷ The spectra also developed shoulders at ~ 550 and ~ 600 nm, corresponding to the 0–1 and 0–0 vibronic transitions of P3HT, respectively.⁷ Similar to the nonannealed

films, the optical absorption of the annealed P3HT:PCBM films increased as the concentration of the PS-AgNPs was increased. Additionally, the absorption intensity differences were higher due to the strong coupling between the PS-AgNPs and the annealed P3HT:PCBM (Figure 4d). Because it is impossible to directly measure the optical absorption after depositing the Al cathode, the reflectance was instead investigated. The reflectance continuously decreased with a greater concentration of PS-AgNPs deposited on P3HT:PCBM after thermal annealing (Figure S12). The progressively decreased reflectance is attributed to increasing optical absorption levels.

To examine the importance of the polymer coating, unfunctionalized AgNPs in as-synthesized aqueous solutions were centrifuged and directly redispersed in MeOH. Without the protective polymer layer, the AgNPs lost their distinct LSPR color, and the solution turned black (Figure S13, inset). As revealed by UV–vis spectroscopy, the solution maintained an absorption peak at $\lambda_{\text{LSPR}} = 485$ nm and gained another peak with a greater intensity at $\lambda = 782$ nm (Figure S13). The new extinction peak is attributed to interparticle plasmonic coupling,^{30,58} which is due to the AgNP aggregation in the solvent. The formation of AgNP aggregates in solutions was confirmed by TEM (Figure S14) with an average aggregated cluster size of 278.2 ± 80.0 nm. The aggregated AgNPs on P3HT:PCBM films were confirmed by SEM (Figure S16). Although the unfunctionalized, aggregated AgNPs enhanced and P3HT:PCBM (Figures S12 and S15), the aggregated AgNPs were detrimental to the performance of OPV devices (Figure S17), demonstrating the importance of a polymer layer on the AgNPs.

Enhancement of Steady-State Photoluminescence. Steady-state photoluminescence (PL) spectroscopy can

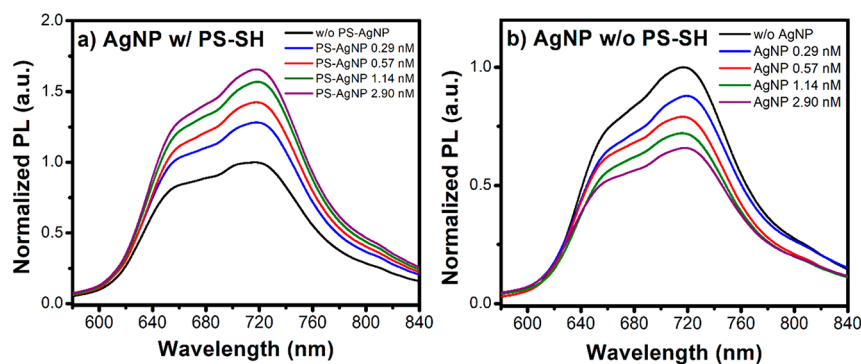


Figure 5. Photoluminescence emission spectra of P3HT films with a layer of (a) PS-AgNPs and (b) AgNPs. The intensities are normalized to the reference films without PS-AgNPs or AgNPs.

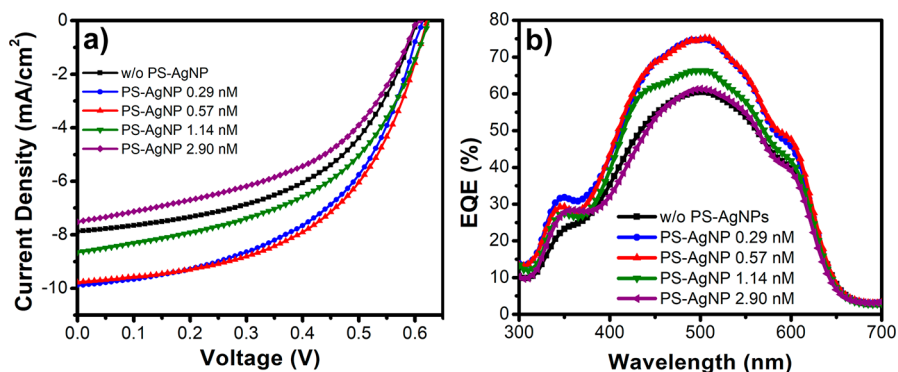


Figure 6. (a) Current density–voltage (J – V) characteristics and (b) the corresponding external quantum efficiency (EQE) of OPV devices.

Table 1. J – V Characteristics of the OPV Devices with PS-AgNPs of Various Concentrations Ranging from 0 to 2.90 nM in the Spin-Coating Solutions^a

PS-AgNPs	J_{sc} (mA/cm ²)	V_{oc} (V)	FF	R_s (Ω -cm ²)	R_{sh} (Ω -cm ²)	PCE (%)	best PCE (%)	% diff
0 nM (ref)	-7.88 ± 0.16	0.62 ± 0.01	0.51 ± 0.02	12.1 ± 2.2	502 ± 159	2.45 ± 0.05	2.61	
0.29 nM	-9.88 ± 0.05	0.62 ± 0.01	0.52 ± 0.01	9.3 ± 0.5	505 ± 67	3.10 ± 0.04	3.14	27
0.57 nM	-9.77 ± 0.11	0.63 ± 0.01	0.53 ± 0.01	11.0 ± 1.1	470 ± 117	3.23 ± 0.13	3.40	32
1.14 nM	-8.65 ± 0.23	0.63 ± 0.01	0.50 ± 0.03	14.1 ± 1.7	330 ± 48	2.69 ± 0.18	2.90	10
2.90 nM	-7.52 ± 0.15	0.61 ± 0.01	0.48 ± 0.02	17.4 ± 2.9	250 ± 32	2.21 ± 0.06	2.27	–10

^aAll values are averaged over at least five devices. The “% diff” is the percentage of the average PCE improvement compared to the reference devices.

indirectly measure the amount of photogenerated excitons at a given PL quantum efficiency.^{25,26,31,33,35,59} When P3HT films (without the PCBM electron acceptor) were excited by a laser at 488 nm, which is a wavelength that P3HT strongly absorbs, the PL intensity increased with the surface density of the PS-AgNPs (Figure 5a). The primary PL peak was at $\lambda = 718$ nm, which corresponds to the singlet exciton emission of P3HT.^{7,29} Higher densities of nanoparticles amplified the LSPR effects and increased the amount of excitons generated by P3HT. The elevated PL intensity is in agreement with the enhanced optical absorption of P3HT:PCBM and pristine P3HT films.

In contrast, the PL intensity of P3HT films with unfunctionalized AgNPs showed an opposite trend; i.e., an increase in the AgNP concentration resulted in a decrease in the PL intensity (Figure 5b). The causes are likely twofold. First, despite that the aggregated AgNPs produced enhanced optical absorption (Figures S10 and S14), the unfunctionalized AgNPs had no insulating polymer layer on the surface and were in direct contact with P3HT, thus providing convenient sites for exciton dissociation, nonradiative recombination, and

photoluminescence quenching.^{31,32} Second, the PL emission spectra of P3HT overlapped the extinction peak of the unfunctionalized AgNPs, which increased the probability of nonradiative recombination by Förster resonance energy transfer.^{29,60} Therefore, it is important to functionalize the AgNPs with appropriate polymers to enhance the PV device performance.

OPV Device Performance. OPV devices were assembled of ITO/PEDOT:PSS/P3HT:PCBM/PS-AgNPs/Al. The current density (J)–voltage (V) curves were measured under 100 mW/cm² AM1.5G illumination. Reference devices without PS-AgNPs were also fabricated and measured. The reference devices had an average short-circuit current density (J_{sc}) of -7.88 mA/cm², an open circuit voltage (V_{oc}) of 0.62 V, a fill factor (FF) of 0.51, and an average power conversion efficiency (PCE) of 2.45% (Figure 6a). After adding a low concentration of the PS-AgNPs, the J – V characteristics improved substantially from the reference devices. At a PS-AgNP concentration of 0.57 nM, the devices performed the best with a J_{sc} of -9.77 mA/cm², a V_{oc} of 0.63 V, a FF of 0.53, and an average PCE of

Table 2. *J*–*V* Characteristics of the OPV Devices with Unfunctionalized AgNPs of Various Concentrations Ranging from 0 to 2.90 nM in the Spin-Coating Solutions^a

AgNP	<i>J</i> _{sc} (mA/cm ²)	<i>V</i> _{oc} (V)	FF	<i>R</i> _s (Ω·cm ²)	<i>R</i> _{sh} (Ω·cm ²)	PCE (%)	best PCE (%)
0 nM (ref)	−7.88 ± 0.16	0.62 ± 0.01	0.51 ± 0.02	12.1 ± 2.2	502 ± 159	2.45 ± 0.05	2.61
0.29 nM	−5.04 ± 0.18	0.59 ± 0.01	0.45 ± 0.01	29.1 ± 0.5	503 ± 36	1.31 ± 0.05	1.36
0.57 nM	−3.59 ± 0.10	0.56 ± 0.02	0.40 ± 0.04	34.9 ± 6.2	367 ± 42	0.81 ± 0.08	0.86
1.14 nM	−2.96 ± 0.22	0.51 ± 0.05	0.36 ± 0.05	39.1 ± 3.0	278 ± 114	0.68 ± 0.29	0.75
2.90 nM	−2.16 ± 0.15	0.50 ± 0.03	0.28 ± 0.02	52.0 ± 14.7	223 ± 35	0.30 ± 0.05	0.37

^aAll values are averaged over at least five devices.

3.23%, which was 32% higher than the average PCE of all reference devices (Table 1). Additionally, the average external quantum efficiency (EQE) spectra peaked at $\lambda = 505$ nm with an efficiency of 75.1%, which was 25% higher than the reference devices (peak EQE = 60.4% at $\lambda = 505$ nm) (Figure 6b). The performance gradually deteriorated when the PS-AgNPs concentration was increased beyond 0.57 nM. At a PS-AgNP concentration of 2.90 nM, the device characteristics dropped below the reference devices. *J*–*V* curves and EQE spectra of OPV devices with unfunctionalized AgNPs were also measured (Figure S17). In contrast, all devices in this case showed worse performance than the reference devices (Table 2).

DISCUSSION

The *R*_{sh} values of the OPV devices were determined by the reciprocal slopes of the *J*–*V* curves at zero bias (i.e., 0 V) following eq 3:

$$R_{\text{sh}} = \left(\frac{dV}{dJ} \right)_{V \rightarrow 0} \quad (3)$$

In an ideal device, *R*_{sh} should be as high as possible. After adding a small amount of the PS-AgNPs (0.29 nM), *R*_{sh} did not change significantly. However, *R*_{sh} decreased continuously as the PS-AgNP concentration was increased from 0.29 to 2.90 nM (Table 1). At a PS-AgNP concentration of 2.90 nM, the average *R*_{sh} values decreased by 50% compared to the reference devices. *R*_{sh} is termed the parallel resistance,⁶¹ which is inversely proportional to the level of leakage current as a result of linear ohmic shunts (i.e., short circuits) and nonlinear local shunts.^{30,62,63} The local shunts, where charge carriers recombine, are usually caused by nanoparticle aggregation,^{30,32,39} poor interface quality, and crystal defects.⁶³ An examination of the PS-AgNPs on the active layer (Figures 3a and 3b) reveals the cause of the decreasing *R*_{sh}. At low PS-AgNP concentrations, the aggregation of the PS-AgNPs was insignificant, and *R*_{sh} was similar to the reference devices. As the nanoparticle concentration was increased, the face-to-face stacking of the PS-AgNPs was unavoidable. The stacked PS-AgNPs behaved as small aggregates and caused local shunts as shown in previous reports.^{30,32,39} In addition, the stacked PS-AgNPs caused surface defects and voids, which immobilized the charge carriers and increased the charge recombination.³⁹ In devices with unfunctionalized AgNPs, the stacking and aggregation were more prevalent and *R*_{sh} dropped more intensely than the OPV devices with PS-AgNPs (Table 2).

The series resistance (*R*_s) was determined by the reciprocal slope of the *J*–*V* curves at voltages much larger than *V*_{oc} following eq 4:

$$R_s = \left(\frac{dV}{dJ} \right)_{V \rightarrow \infty} \quad (4)$$

In contrast to *R*_{sh}, *R*_s should be as low as possible in an ideal device. *R*_s decreased favorably by ~25% after adding a small amount of PS-AgNPs (0.29 nM); then it increased as the PS-AgNP concentration was increased from 0.29 to 2.90 nM (Table 1). At a PS-AgNP concentration of 2.90 nM, *R*_s increased by 43% compared to the reference devices. *R*_s is the combined resistance of the active layer, electrodes, and interfacial contacts.⁶⁴ The decrease in *R*_s after adding 0.29 nM of PS-AgNPs is attributed to a beneficial drop in the contact resistance between the active layer and the cathode, since all other parameters were constant such as the device processing conditions, the active layer thickness, and the electrode materials. At low PS-AgNP concentrations, the resistance most likely decreased due to the increased surface roughness of the active layer (Figure S10), which led to an increase of the interfacial surface area between the active layer and the cathode.^{65,66} Although the polymer layer largely insulated the AgNPs,⁴⁰ it was shown in previous reports that due to the strong citrate adsorption on NPs, a complete citrate-to-thiol ligand exchange is difficult and a small portion of the total particle surface area is possibly uninsulated.⁵⁸ As a result, there was possible charge injection⁶⁶ from P3HT:PCBM to the PS-AgNPs and subsequent charge transport^{36,42} from the PS-AgNPs to the aluminum electrodes. Although charge injection might remain in devices with stacked PS-AgNPs of high concentrations and aggregated unfunctionalized AgNPs, the average *R*_s values increased disadvantageously due to the creation of defects, voids, and decreased contact between the active layer and the cathode.³⁹ Essentially, the greater roughness and the lack of uniformity characteristic of the aggregated unfunctionalized AgNPs prohibited effective contact between the active layer and metallic cathode.

FF mostly depends on the resistances *R*_{sh} and *R*_s.⁶⁷ To maximize the FF, the *R*_s and *R*_{sh} should be as low and as high as possible, respectively. At low PS-AgNP concentrations of 0.29 and 0.57 nM, the *R*_s values were lower than that of the reference devices, and thus their FF values were higher. In devices with high PS-AgNP concentrations of 1.14 and 2.90 nM or unfunctionalized AgNPs, *R*_s increased and *R*_{sh} decreased and thus FF decreased.

*J*_{sc} is primarily related to *R*_s, optical absorption, film morphology, and charge carrier mobility.^{1–6,8,10,64,68} The optical absorption of the OPV devices was enhanced by the nanoparticle LSPR (Figure 4). In the devices with PS-AgNPs, the *J*_{sc} was mainly dependent on a competition between the optical absorption and *R*_s. Thanks to the improved optical absorption and the lowest *R*_s, the OPV devices with the lowest PS-AgNP concentration of 0.29 nM exhibited the highest *J*_{sc}, which was 25% more than the reference devices. When the PS-

AgNP concentration was above 0.29 nM, however, the increasing R_s overwhelmed the effect of the increasing optical absorption and thus J_{sc} continuously declined. The effect of R_s was more prominent in the devices with unfunctionalized AgNPs, where J_{sc} substantially degraded as the AgNP concentration was increased. EQE exhibited a similar trend: EQE increased significantly compared to the reference devices when the PS-AgNP concentration was at 0.29 or 0.57 nM; it declined continuously when the concentration was further increased to 2.90 nM. The EQE changes ($\Delta EQE\%$) showed apparent enhancements in the vicinity of the PS-AgNP λ_{LSPR} (Figure S18). Additionally, the out-of-plane quadrupole peak of the PS-AgNPs ($\lambda = 339$ nm) matched closely to the absorption peak of PCBM ($\lambda \approx 340$ nm), which led to a substantial EQE enhancement in this wavelength range. Besides the relation of absorption enhancements, the enhanced R_s values at the low PS-AgNP concentrations (0.29 and 0.57 nM) enhanced the EQE broadly across the P3HT:PCBM absorption spectrum. An opposite effect was observed in devices with high PS-AgNP concentrations (1.14 and 2.90 nM). For devices with the unfunctionalized AgNPs, both EQE and J_{sc} deteriorated substantially due to the increase in R_s . Because both optical absorption and charge transport influence the EQE, these two factors together impact the changes in the EQE spectra.

V_{oc} is determined by the difference between the lowest unoccupied molecular orbital (LUMO) of the acceptor and the highest occupied molecular orbital (HOMO) of the donor along with the voltage losses due to band bending at the electrodes,^{57,69} energetic disorder,^{5,69} and charge recombination.^{5,69} It is reported that trap-assisted recombination, which could be induced by the ligand-capped AgNPs, causes drops in V_{oc} .^{29,32} In addition, since R_{sh} is inversely correlated to the charge recombination level, a decrease in R_{sh} can deteriorate the V_{oc} .^{39,67} especially at low light intensities where the leakage current dominates.⁶¹ After adding PS-AgNPs, the V_{oc} showed only subtle variations, mainly associated with the uncertainties of the average values. Contrastingly, the V_{oc} steadily declined after adding an increasing amount of unfunctionalized AgNPs. The defects and voids created by the unfunctionalized AgNP aggregates enhanced the recombination rates and reduced the shunt resistance,³⁹ which ultimately resulted in a severely degraded V_{oc} .

FF, J_{sc} , and V_{oc} collectively determine the PCE of an OPV device. At a PS-AgNP concentration of 0.57 nM, the devices showed the highest combined effects of FF, J_{sc} , and V_{oc} . As a result, the PCE increased by 32% compared to the reference devices. With a PS-AgNP concentration of 0.29 nM, the devices showed a slightly lower PCE increase of 27% due to the marginally lower FF and V_{oc} . The manner in which the optical absorption and R_s influence J_{sc} and PCE is convoluted and lacks a formal relationship. Therefore, we utilize the quantitative enhancements to approximate the proportion of these effects. In Table 3, the “single pass %” represents the light absorption for a single optical pass through the active layer. The “double pass %” accounts for not only the initial single optical pass but also the second pass as the light is fully reflected off the Al cathode and transmitted back through the active layer. At the lowest PS-AgNP concentration (0.29 nM), the R_s enhancement was significantly more prominent than the optical absorption enhancement (23.1% versus 7.7%, respectively), which means that the R_s is the dominant factor for the PCE increases. However, at the PS-AgNP concentration of

Table 3. Optical Absorption and Electrical Enhancements of the OPV Devices Compared with the Reference Devices (with 0% PS-AgNPs)^a

PS-AgNPs	single pass %	double pass %	R_s (%)	J_{sc} (%)	V_{oc} (%)	FF (%)
0.29 nM	3.8	7.7	23.3	25.3	0	2.0
0.57 nM	5.5	10.9	8.9	24.0	1.6	3.9

^aThe optical absorption is designated as “single pass %” and “double pass %”, where double pass refers to the total absorption after light is transmitted through the device and fully reflected back by the Al cathode.

0.57 nM, the optical absorption enhancement is larger than the R_s (10.9% versus 9.1%, respectively). When the PS-AgNP concentration was above 0.57 nM, PCE decreased continuously due to the deteriorated characteristics of FF, J_{sc} , and V_{oc} . At a PS-AgNP concentration of 2.90 nM, the PCE was even lower than the reference devices due to the worse FF, J_{sc} , and V_{oc} . In OPV devices with unfunctionalized AgNPs, the FF, J_{sc} , and V_{oc} all decreased, and the PCE values were low at all concentrations compared to the reference devices. Even at the lowest concentration of 0.29 nM, the AgNPs caused a PCE decrease by 47%. The continuously declined performance with an increasing concentration of the AgNPs highlights that unfunctionalized AgNPs are detrimental to the OPVs, despite the enhanced optical absorption. The polymer layer effectively insulated the PS-AgNPs, minimized the nanoparticle aggregation, and provided significant enhancements to the PCE of the OPV devices.

CONCLUSIONS

We have shown that the polymer-functionalized PS-AgNPs effectively increase the optical absorption and improve the power conversion efficiency of organic photovoltaics. We demonstrate that an insulating polymer layer on the plasmonic nanoparticles, such as polystyrene, is essential for reducing the detrimental effects such as exciton quenching and charge trapping, even when the nanoparticles are placed between the active layer and the cathode. The polystyrene layer on the nanoparticles also enables their stable dispersion in organic solvents and effective spin-coating on the active layer. To effectively improve the light absorption, the λ_{LSPR} of the PS-AgNPs are coupled to the λ_{max} of the active layer. As the concentration of the PS-AgNPs is increased, the light absorption of the active layer is enhanced. The power conversion efficiency, however, increases only at low PS-AgNP concentrations, peaks at a concentration of 0.57 nM (32% improvement compared to the reference devices), and then decreases at high concentrations. Unfunctionalized AgNPs deteriorate the performances of the OPV devices regardless of the concentration.

Future work involves varying the polymer molecular weight and the surface density of the polymer chains on the nanoparticles, which will elucidate how the polymer layer influences the LSPR enhancement effect of the AgNPs. Additionally, the “graft-from” method can be used to anchor polymer chains directly onto the AgNPs, which can potentially maximize the insulation effect of the polymer layer. The polymer layer on the plasmonic nanoparticles is critical for insulating the nanoparticles and minimizing their aggregation, which can inspire future designs of plasmonic nanoparticles for PV applications. The strategy of utilizing polymer-function-

alized plasmonic nanoparticles to enhance the optical absorption is expected to be applicable to virtually any thin-film PV technology.

■ ASSOCIATED CONTENT

Supporting Information

The Supporting Information is available free of charge on the ACS Publications website at DOI: 10.1021/acsaeam.8b01860.

Additional SEM, TEM, UV–vis–NIR characterizations, NMR, schematics, and other plots (PDF)

■ AUTHOR INFORMATION

Corresponding Authors

*E-mail gliul@vt.edu; phone (540) 231-8241.

*E-mail rheflin@vt.edu; phone (540) 231-4504.

ORCID

Assad U. Khan: 0000-0001-6455-3219

Guoliang Liu: 0000-0002-6778-0625

Notes

The authors declare no competing financial interest.

■ ACKNOWLEDGMENTS

G.L. appreciates the National Science Foundation CAREER Award. This material is based upon work supported by the National Science Foundation under Grant DMR-1752611. This work was partially supported by the AFOSR through Grant FA9550-17-1-0341 and DURIP funding (FA9550-16-1-0358). The authors gracefully acknowledge David Clark and Bill Reynolds from the Materials Science and Engineering Department at Virginia Tech for their assistance in materials funding. The authors also acknowledge several individuals who assisted with the experimental methods in this work, namely Eric Carlson, Don Leber from the Micro and Nano fabrication lab, and Michael Bouchard, who helped with the repair and maintenance of the thermal evaporator system. The authors acknowledge Steve McCartney and Christopher Winkler in the nanoscale characterization and fabrication laboratory (NCFL) at Virginia Tech ICTAS for their microscopy support. The authors acknowledge Min Gao for graciously allowing the authors to use the AFM in his laboratory.

■ REFERENCES

- (1) Lu, L.; Zheng, T.; Wu, Q.; Schneider, A. M.; Zhao, D.; Yu, L. Recent Advances in Bulk Heterojunction Polymer Solar Cells. *Chem. Rev.* **2015**, *115*, 12666–12731.
- (2) Li, G.; Zhu, R.; Yang, Y. Polymer Solar Cells. *Nat. Photonics* **2012**, *6*, 153–161.
- (3) Zhao, F.; Dai, S.; Wu, Y.; Zhang, Q.; Wang, J.; Jiang, L.; Ling, Q.; Wei, Z.; Ma, W.; You, W.; Wang, C.; Zhan, X. Single-Junction Binary-Blend Nonfullerene Polymer Solar Cells with 12.1% Efficiency. *Adv. Mater.* **2017**, *29*, 1700144.
- (4) Zhao, J.; Li, Y.; Yang, G.; Jiang, K.; Lin, H.; Ade, H.; Ma, W.; Yan, H. Efficient Organic Solar Cells Processed from Hydrocarbon Solvents. *Nat. Energy* **2016**, *1*, 15027.
- (5) He, Z.; Xiao, B.; Liu, F.; Wu, H.; Yang, Y.; Xiao, S.; Wang, C.; Russell, T. P.; Cao, Y. Single-Junction Polymer Solar Cells with High Efficiency and Photovoltage. *Nat. Photonics* **2015**, *9*, 174–179.
- (6) Li, G.; Shrotiyra, V.; Huang, J.; Yao, Y.; Moriarty, T.; Emery, K.; Yang, Y. High-Efficiency Solution Processable Polymer Photovoltaic Cells by Self-Organization of Polymer Blends. *Nat. Mater.* **2005**, *4*, 864–868.
- (7) Marsh, R. A.; Hodgkiss, J. M.; Albert-Seifried, S.; Friend, R. H. Effect of Annealing on P3HT:PCBM Charge Transfer and Nanoscale

Morphology Probed by Ultrafast Spectroscopy. *Nano Lett.* **2010**, *10*, 923–930.

(8) Wang, T.; Pearson, A. J.; Lidzey, D. G.; Jones, R. A. Evolution of Structure, Optoelectronic Properties, and Device Performance of Polythiophene: Fullerene Solar Cells During Thermal Annealing. *Adv. Funct. Mater.* **2011**, *21*, 1383–1390.

(9) Erb, T.; Zhokhavets, U.; Gobsch, G.; Raleva, S.; Stühn, B.; Schilinsky, P.; Waldauf, C.; Brabec, C. J. Correlation between Structural and Optical Properties of Composite Polymer/Fullerene Films for Organic Solar Cells. *Adv. Funct. Mater.* **2005**, *15*, 1193–1196.

(10) Li, H.; Tang, H.; Li, L.; Xu, W.; Zhao, X.; Yang, X. Solvent-Soaking Treatment Induced Morphology Evolution in P3HT/PCBM Composite Films. *J. Mater. Chem.* **2011**, *21*, 6563–6568.

(11) Atwater, H. A.; Polman, A. Plasmonics for Improved Photovoltaic Devices. *Nat. Mater.* **2010**, *9*, 205–213.

(12) Pastoriza-Santos, I.; Liz-Marzán, L. M. Colloidal Silver Nanoplates. State of the Art and Future Challenges. *J. Mater. Chem.* **2008**, *18*, 1724–1737.

(13) Kelly, K. L.; Coronado, E.; Zhao, L. L.; Schatz, G. C. The Optical Properties of Metal Nanoparticles: The Influence of Size, Shape, and Dielectric Environment. *J. Phys. Chem. B* **2003**, *107*, 668–677.

(14) Khan, A. U.; Scraggs, C.; Hicks, D.; Liu, G. Two-Dimensional Plasmonic Nanoparticle as a Nanoscale Sensor to Probe Polymer Brush Formation. *Anal. Chem.* **2017**, *89*, 7541–7548.

(15) Khan, A. U.; Zhao, S.; Liu, G. Key Parameter Controlling the Sensitivity of Plasmonic Metal Nanoparticles: Aspect Ratio. *J. Phys. Chem. C* **2016**, *120*, 19353–19364.

(16) Kulkarni, A. P.; Noone, K. M.; Munechika, K.; Guyer, S. R.; Ginger, D. S. Plasmon-Enhanced Charge Carrier Generation in Organic Photovoltaic Films Using Silver Nanoprisms. *Nano Lett.* **2010**, *10*, 1501–1505.

(17) Stratakis, E.; Kymakis, E. Nanoparticle-Based Plasmonic Organic Photovoltaic Devices. *Mater. Today* **2013**, *16*, 133–146.

(18) Ferry, V. E.; Verschuuren, M. A.; Li, H. B.; Verhagen, E.; Walters, R. J.; Schropp, R. E.; Atwater, H. A.; Polman, A. Light Trapping in Ultrathin Plasmonic Solar Cells. *Opt. Express* **2010**, *18*, A237–A245.

(19) Baek, S.-W.; Noh, J.; Lee, C.-H.; Kim, B.; Seo, M.-K.; Lee, J.-Y. Plasmonic Forward Scattering Effect in Organic Solar Cells: A Powerful Optical Engineering Method. *Sci. Rep.* **2013**, *3*, 1726.

(20) Lindquist, N. C.; Nagpal, P.; McPeak, K. M.; Norris, D. J.; Oh, S.-H. Engineering Metallic Nanostructures for Plasmonics and Nanophotonics. *Rep. Prog. Phys.* **2012**, *75*, 036501.

(21) West, P. R.; Ishii, S.; Naik, G. V.; Emani, N. K.; Shalae, V. M.; Boltasseva, A. Searching for Better Plasmonic Materials. *Laser Photonics Rev.* **2010**, *4*, 795–808.

(22) Haes, A. J.; Haynes, C. L.; McFarland, A. D.; Schatz, G. C.; Van Duyne, R. P.; Zou, S. Plasmonic Materials for Surface-Enhanced Sensing and Spectroscopy. *MRS Bull.* **2005**, *30*, 368–375.

(23) Fung, D. D.; Qiao, L.; Choy, W. C.; Wang, C.; Sha, W. E. I.; Xie, F.; He, S. Optical and Electrical Properties of Efficiency Enhanced Polymer Solar Cells with Au Nanoparticles in a PEDOT-PSS Layer. *J. Mater. Chem.* **2011**, *21*, 16349–16356.

(24) Yao, K.; Salvador, M.; Chueh, C. C.; Xin, X. K.; Xu, Y. X.; deQuilettes, D. W.; Hu, T.; Chen, Y.; Ginger, D. S.; Jen, A. K. Y. A General Route to Enhance Polymer Solar Cell Performance Using Plasmonic Nanoprisms. *Adv. Energy Mater.* **2014**, *4*, 1400206.

(25) Wu, J.-L.; Chen, F.-C.; Hsiao, Y.-S.; Chien, F.-C.; Chen, P.; Kuo, C.-H.; Huang, M. H.; Hsu, C.-S. Surface Plasmonic Effects of Metallic Nanoparticles on the Performance of Polymer Bulk Heterojunction Solar Cells. *ACS Nano* **2011**, *5*, 959–967.

(26) Yang, Y.; Lin, X.; Qing, J.; Zhong, Z.; Ou, J.; Hu, C.; Chen, X.; Zhou, X.; Chen, Y. Enhancement of Short-Circuit Current Density in Polymer Bulk Heterojunction Solar Cells Comprising Plasmonic Silver Nanowires. *Appl. Phys. Lett.* **2014**, *104*, 123302.

(27) Ren, X.; Cheng, J.; Zhang, S.; Li, X.; Rao, T.; Huo, L.; Hou, J.; Choy, W. C. High Efficiency Organic Solar Cells Achieved by the

Simultaneous Plasmon-Optical and Plasmon-Electrical Effects from Plasmonic Asymmetric Modes of Gold Nanostars. *Small* **2016**, *12*, 5200–5207.

(28) Kim, H.; Nam, S.; Lee, H.; Woo, S.; Ha, C.-S.; Ree, M.; Kim, Y. Influence of Controlled Acidity of Hole-Collecting Buffer Layers on the Performance and Lifetime of Polymer: Fullerene Solar Cells. *J. Phys. Chem. C* **2011**, *115*, 13502–13510.

(29) Wu, B.; Wu, X.; Guan, C.; Tai, K. F.; Yeow, E. K. L.; Fan, H. J.; Mathews, N.; Sum, T. C. Uncovering Loss Mechanisms in Silver Nanoparticle-Blended Plasmonic Organic Solar Cells. *Nat. Commun.* **2013**, *4*, 4.

(30) Topp, K.; Borchert, H.; Johnen, F.; Tunc, A.; Knipper, M.; Von Hauff, E.; Parisi, J.; Al-Shamery, K. Impact of the Incorporation of Au Nanoparticles into Polymer/Fullerene Solar Cells. *J. Phys. Chem. A* **2010**, *114*, 3981–3989.

(31) Du, P.; Jing, P.; Li, D.; Cao, Y.; Liu, Z.; Sun, Z. Plasmonic Ag@Oxide Nanoprisms for Enhanced Performance of Organic Solar Cells. *Small* **2015**, *11*, 2454–2462.

(32) Xue, M.; Li, L.; Tremolet de Villers, B. J.; Shen, H.; Zhu, J.; Yu, Z.; Stieg, A. Z.; Pei, Q.; Schwartz, B. J.; Wang, K. L. Charge-Carrier Dynamics in Hybrid Plasmonic Organic Solar Cells with Ag Nanoparticles. *Appl. Phys. Lett.* **2011**, *98*, 253302.

(33) Kymakis, E.; Spyropoulos, G. D.; Fernandes, R.; Kakavelakis, G.; Kanaras, A. G.; Stratakis, E. Plasmonic Bulk Heterojunction Solar Cells: The Role of Nanoparticle Ligand Coating. *ACS Photonics* **2015**, *2*, 714–723.

(34) Shen, W.; Tang, J.; Yang, R.; Cong, H.; Bao, X.; Wang, Y.; Wang, X.; Huang, Z.; Liu, J.; Huang, L.; et al. Enhanced Efficiency of Polymer Solar Cells by Incorporated Ag-SiO₂ Core-Shell Nanoparticles in the Active Layer. *RSC Adv.* **2014**, *4*, 4379–4386.

(35) Spyropoulos, G. D.; Stylianakis, M. M.; Stratakis, E.; Kymakis, E. Organic Bulk Heterojunction Photovoltaic Devices with Surfactant-Free Au Nanoparticles Embedded in the Active Layer. *Appl. Phys. Lett.* **2012**, *100*, 213904.

(36) Kalfagiannis, N.; Karagiannidis, P.; Pitsalidis, C.; Panagiotopoulos, N.; Gravalidis, C.; Kassavetis, S.; Patsalas, P.; Logothetidis, S. Plasmonic Silver Nanoparticles for Improved Organic Solar Cells. *Sol. Energy Mater. Sol. Cells* **2012**, *104*, 165–174.

(37) Xie, F. X.; Choy, W. C.; Sha, W. E. I.; Zhang, D.; Zhang, S.; Li, X.; Leung, C. W.; Hou, J. Enhanced Charge Extraction in Organic Solar Cells through Electron Accumulation Effects Induced by Metal Nanoparticles. *Energy Environ. Sci.* **2013**, *6*, 3372–3379.

(38) Zhang, D.; Choy, W. C.; Xie, F.; Sha, W. E.; Li, X.; Ding, B.; Zhang, K.; Huang, F.; Cao, Y. Plasmonic Electrically Functionalized TiO₂ for High-Performance Organic Solar Cells. *Adv. Funct. Mater.* **2013**, *23*, 4255–4261.

(39) Li, P.; Jiu, T.; Tang, G.; Wang, G.; Li, J.; Li, X.; Fang, J. Solvents Induced ZnO Nanoparticles Aggregation Associated with Their Interfacial Effect on Organic Solar Cells. *ACS Appl. Mater. Interfaces* **2014**, *6*, 18172–18179.

(40) Butcher, D. P.; Wadams, R. C.; Drummy, L.; Koerner, H.; Bailey, C.; Scheltens, F.; McComb, D.; Fabris, L.; Durstock, M. F.; Tabor, C. Controlled Dispersion of Polystyrene-Capped Au Nanoparticles in P3HT:PC₆₁BM and Consequences Upon Active Layer Nanostructure. *J. Polym. Sci., Part B: Polym. Phys.* **2016**, *54*, 709–720.

(41) Woo, Y. J.; Park, K. H.; Park, O. O.; Wang, D. H. Dispersion Control of Ag Nanoparticles in Bulk-Heterojunction for Efficient Organic Photovoltaic Devices. *Org. Electron.* **2015**, *16*, 118–125.

(42) Li, X.; Choy, W. C. H.; Lu, H.; Sha, W. E.; Ho, A. H. P. Efficiency Enhancement of Organic Solar Cells by Using Shape-Dependent Broadband Plasmonic Absorption in Metallic Nanoparticles. *Adv. Funct. Mater.* **2013**, *23*, 2728–2735.

(43) Lombardo, M. T.; Pozzo, L. D. Clusters and Inverse Emulsions from Nanoparticle Surfactants in Organic Solvents. *Langmuir* **2015**, *31*, 1344–1352.

(44) Bokern, S.; Getze, J.; Agarwal, S.; Greiner, A. Polymer Grafted Silver and Copper Nanoparticles with Exceptional Stability against Aggregation by a High Yield One-Pot Synthesis. *Polymer* **2011**, *52*, 912–920.

(45) Pletsch, H.; Peng, L.; Mitschang, F.; Schaper, A.; Hellwig, M.; Nette, D.; Seubert, A.; Greiner, A.; Agarwal, S. Ultrasound-Mediated Synthesis of High-Molecular Weight Polystyrene-Grafted Silver Nanoparticles by Facile Ligand Exchange Reactions in Suspension. *Small* **2014**, *10*, 201–208.

(46) Aherne, D.; Ledwith, D. M.; Gara, M.; Kelly, J. M. Optical Properties and Growth Aspects of Silver Nanoprisms Produced by a Highly Reproducible and Rapid Synthesis at Room Temperature. *Adv. Funct. Mater.* **2008**, *18*, 2005–2016.

(47) Khan, A. U.; Zhou, Z.; Krause, J.; Liu, G. Poly (Vinylpyrrolidone)-Free Multistep Synthesis of Silver Nanoplates with Plasmon Resonance in the near Infrared Range. *Small* **2017**, *13*, 1701715.

(48) Nishi, H.; Kobatake, S. Reduction Reaction to Thiol Group of Dithiobenzoate End Group in Polystyrene Polymerized by Reversible Addition-Fragmentation Chain Transfer. *Chem. Lett.* **2008**, *37*, 630–631.

(49) Galati, E.; Tebbe, M.; Querejeta-Fernández, A.; Xin, H. L.; Gang, O.; Zhulina, E. B.; Kumacheva, E. Shape-Specific Patterning of Polymer-Functionalized Nanoparticles. *ACS Nano* **2017**, *11*, 4995–5002.

(50) Pedersen, J.; Schurtenberger, P. Static Properties of Polystyrene in Semidilute Solutions: A Comparison of Monte Carlo Simulation and Small-Angle Neutron Scattering Results. *EPL* **1999**, *45*, 666–672.

(51) Guo, Y.; Khan, A. U.; Cao, K.; Liu, G. Janus Plasmonic Silver Nanoplatelets for Interface Stabilization. *ACS Applied Nano Materials* **2018**, *1*, 5377–5381.

(52) Rang, M.; Jones, A. C.; Zhou, F.; Li, Z.-Y.; Wiley, B. J.; Xia, Y.; Raschke, M. B. Optical near-Field Mapping of Plasmonic Nanoprisms. *Nano Lett.* **2008**, *8*, 3357–3363.

(53) Haes, A. J.; Zou, S.; Schatz, G. C.; Van Duyne, R. P. Nanoscale Optical Biosensor: Short Range Distance Dependence of the Localized Surface Plasmon Resonance of Noble Metal Nanoparticles. *J. Phys. Chem. B* **2004**, *108*, 6961–6968.

(54) Spin Coating: A Guide to Theory and Techniques; <https://www.ossila.com/pages/spin-coating> (accessed December 17, 2018).

(55) Gibbard, H. F.; Creek, J. L. Vapor Pressure of Methanol from 288.15 to 337.65K. *J. Chem. Eng. Data* **1974**, *19*, 308–310.

(56) Cui, X.; Chen, G.; Han, X. Experimental Vapor Pressure Data and a Vapor Pressure Equation for N, N-Dimethylformamide. *J. Chem. Eng. Data* **2006**, *51*, 1860–1861.

(57) Bartesaghi, D.; del Carmen Pérez, I.; Kniepert, J.; Roland, S.; Turbiez, M.; Neher, D.; Koster, L. J. A. Competition between Recombination and Extraction of Free Charges Determines the Fill Factor of Organic Solar Cells. *Nat. Commun.* **2015**, *6*, 7083.

(58) Park, J.-W.; Shumaker-Parry, J. S. Strong Resistance of Citrate Anions on Metal Nanoparticles to Desorption under Thiol Functionalization. *ACS Nano* **2015**, *9*, 1665–1682.

(59) Piris, J.; Dykstra, T. E.; Bakulin, A. A.; Loosdrecht, P. H. v.; Knulst, W.; Trinh, M. T.; Schins, J. M.; Siebbeles, L. D. Photogeneration and Ultrafast Dynamics of Excitons and Charges in P3HT/PCBM Blends. *J. Phys. Chem. C* **2009**, *113*, 14500–14506.

(60) Hodgkiss, J. M.; Albert-Seifried, S.; Rao, A.; Barker, A. J.; Campbell, A. R.; Marsh, R. A.; Friend, R. H. Exciton-Charge Annihilation in Organic Semiconductor Films. *Adv. Funct. Mater.* **2012**, *22*, 1567–1577.

(61) Proctor, C. M.; Nguyen, T.-Q. Effect of Leakage Current and Shunt Resistance on the Light Intensity Dependence of Organic Solar Cells. *Appl. Phys. Lett.* **2015**, *106*, 083301.

(62) Li, Y. *Three Dimensional Solar Cells Based on Optical Confinement Geometries*; Springer Science & Business Media: 2012.

(63) Breitenstein, O.; Rakotoniaina, J.; Al Rifai, M. H.; Werner, M. Shunt Types in Crystalline Silicon Solar Cells. *Prog. Photovoltaics* **2004**, *12*, 529–538.

(64) Servaites, J. D.; Yeganeh, S.; Marks, T. J.; Ratner, M. A. Efficiency Enhancement in Organic Photovoltaic Cells: Consequences of Optimizing Series Resistance. *Adv. Funct. Mater.* **2010**, *20*, 97–104.

(65) Park, H. I.; Lee, S.; Lee, J. M.; Nam, S. A.; Jeon, T.; Han, S. W.; Kim, S. O. High Performance Organic Photovoltaics with Plasmonic-Coupled Metal Nanoparticle Clusters. *ACS Nano* **2014**, *8*, 10305–10312.

(66) Salvador, M.; MacLeod, B. A.; Hess, A.; Kulkarni, A. P.; Munchika, K.; Chen, J. I.; Ginger, D. S. Electron Accumulation on Metal Nanoparticles in Plasmon-Enhanced Organic Solar Cells. *ACS Nano* **2012**, *6*, 10024–10032.

(67) Luque, A.; Hegedus, S. *Handbook of Photovoltaic Science and Engineering*; John Wiley & Sons: 2011.

(68) Gupta, D.; Bag, M.; Narayan, K. Correlating Reduced Fill Factor in Polymer Solar Cells to Contact Effects. *Appl. Phys. Lett.* **2008**, *92*, 093301.

(69) Collins, S. D.; Proctor, C. M.; Ran, N. A.; Nguyen, T. Q. Understanding Open-Circuit Voltage Loss through the Density of States in Organic Bulk Heterojunction Solar Cells. *Adv. Energy Mater.* **2016**, *6*, 1501721.